Nonlinear analysis of circular high strength concrete-filled stainless steel tubular slender beam-columns

Nonlinear analysis of circular high strength concrete-filled stainless steel tubular slender beam-columns

Vipulkumar Ishvarbhai Patel[a], Qing Quan Liang[b,*], Muhammad N. S. Hadi[c]

[a] *School of Engineering and Mathematical Sciences, College of Science, Health and Engineering, La Trobe University, PO Box 199, Bendigo, VIC 3552, Australia*
[b] *College of Engineering and Science, Victoria University, PO Box 14428, Melbourne, VIC 8001, Australia*
[c] *School of Civil, Mining and Environmental Engineering, University of Wollongong, Wollongong, NSW 2522, Australia*

ABSTRACT

Concrete-filled stainless steel tubular (CFSST) slender columns are increasingly used in composite structures owing to their distinguished features, such as aesthetic appearance, high corrosion resistance, high durability and ease of maintenance. Currently, however, there is a lack of an accurate and efficient numerical model that can be utilized to determine the performance of circular CFSST slender columns. This paper describes a nonlinear fiber-based model proposed for computing the deflection and axial load-moment strength interaction responses of eccentrically loaded circular high-strength CFSST slender columns. The fiber-based model incorporates the accurate three-stage stress-strain relations of stainless steels, accounting for different strain hardening characteristics in tension and compression. The material and geometric nonlinearities as well as concrete confinement are included in the computational procedures. Existing experimental results on axially loaded CFSST slender columns are utilized to verify the proposed fiber-based model. A parametric study is conducted to examine the performance of high-strength slender CFSST beam-columns with various geometric and material parameters. It is shown that the fiber-based analysis technique

[*]Corresponding author. Tel.: 61 3 9919 4134.
E-mail address: Qing.Liang@vu.edu.au (Q. Q. Liang)

developed can accurately capture the experimentally observed performance of circular high-strength CFSST slender columns. The results obtained indicate that increasing the eccentricity ratio, column slenderness ratio and diameter-to-thickness ratio remarkably decreases the initial flexural stiffness and ultimate axial strength of CFSST columns, but considerably increases their displacement ductility. Moreover, an increase in concrete compressive strength increases the flexural stiffness and ultimate axial strength of CFSST columns; however, it decreases their ductility. Furthermore, the ultimate axial strength of CFST slender columns is found to increase by using stainless steel tubes with higher proof stresses.

Keywords: Concrete-filled stainless steel tubes; High strength; Nonlinear analysis; Slender composite columns.

1. Introduction

Concrete-filled steel tubular (CFST) slender columns made of carbon steel tubes have been widely used in composite buildings, arch bridges, offshore structures and electricity pylons [1]. Despite the initial high cost of stainless steel, CFSST columns are increasingly used in modern engineering structures in recent years. The reason for this is that CFSST columns not only have the structural advantages of conventional CFST columns, but also possess aesthetic appearance, high corrosion resistance, high durability and ease of maintenance. To reduce the cost of CFSST columns, high-strength concrete can be utilized to construct CFSST columns. However, the performance of eccentrically loaded circular high-strength CFSST slender columns has not been investigated experimentally and numerically. Moreover, design rules for this type of columns have not been provided in international standards, such as Eurocode 4 [2], LRFD [3], ACI 318-11 [4] and AS 5100.6 [5]. Therefore, there is a need for developing

an accurate and efficient numerical model that can be employed to simulate the responses of circular CFSST slender columns under eccentric loading.

Experiments on high-strength CFST slender columns have been undertaken by researchers in the past [6-22]. However, experimental studies of circular high-strength CFSST columns are very limited [23]. Young and Ellobody [24] carried out experiments on high-strength square and rectangular stainless steel tubular short columns made of concrete with strengths ranging from 40 to 80 MPa. Circular and square CFSST short columns subjected to axial loading were tested to failure by Lam and Gardner [25]. These CFSST columns were fabricated using normal strength stainless steel tubes and concrete with strengths varying from 30 to 100 MPa. Uy et al. [26] described experimental procedures and observations on short circular and rectangular CFSST columns, which were constructed by low strength concrete and normal strength stainless steel tubes and slender columns made of normal strength stainless steel tubes and normal or high strength concrete. Ellobody and Ghazy [27] tested circular plain CFSST short columns and fiber reinforced CFSST slender beam-columns. Experimental studies on rectangular CFSST slender columns under biaxial loads were reported by Tokgoz [28]. It was found that short CFSST columns had typical failure modes of the outward local buckling of stainless steel tubes and concrete crushing while CFSST slender columns generally failed by global column buckling.

Computational models have been presented for the inelastic analysis of eccentrically loaded CFST slender columns fabricated by high-strength materials [29-38]. However, the strength and behavior of eccentrically loaded circular high-strength CFSST slender columns have not been investigated by inelastic analysis procedures. Ellobody and Young [39], Tao et al. [40] and Hassanein et al. [41] utilized commercial finite element analysis software ABAQUS to

simulate short circular and square CFSST columns under axial compression. The structural responses of slender circular stainless steel tubular beam-columns filled with fiber reinforced concrete were investigated by Ellobody [42] using ABAQUS. In these studies, either the measured stress-strain curves or the two-stage stress-strain relations given by Rasmussen [43] were used to simulate the material behavior of stainless steels. Quach et al. [44] reported that stainless steel has different strain hardening characteristics in compression and tension [45] and the two-stage stress-strain laws given by Rasmussen [43] were based on the tension coupon test results, which underestimates the ultimate compressive strength of stainless steels. Patel et al. [46] incorporated the accurate three-stage stress-strain relations given by Quach et al. [44] and Abdella et al. [47] for stainless steels in the fiber element modeling of short circular CFSST columns. The numerical solutions obtained were shown to agree well with experimental results.

The axial load-moment strength interaction behavior of circular high-strength CFSST slender columns under eccentric loads has not been studied by inelastic analysis techniques. In this paper, an efficient nonlinear fiber-based model is formulated for modeling the load-deflection responses of circular high-strength CFSST slender columns as well as their axial load-moment strength interaction curves. The accurate three-stage stress-strain relations of stainless steels with different strain hardening behaviors in tension and compression given by Quach et al. [44] and Abdella et al. [47] are implemented in the fiber-based model for the first time. The nonlinear fiber-based analysis technique is validated by existing experimental data. The verified fiber-based model is employed to determine the effects of important geometric and material parameters on the performance of eccentrically loaded circular CFSST slender columns of made of high-strength materials.

2. Nonlinear fiber-based model

2.1. Cross-sectional analysis

The fiber element analysis method [34, 48] is used in the present study to discretize the cross-section of a circular CFSST column as illustrated in Fig. 1. The method assumes that: (a) there is a perfect bond at the interface between the stainless steel tube and concrete; (b) plane section remains plane after deformation; (c) the local buckling of the stainless steel tube is not included; (d) concrete confinement is taken into account; (e) the effect of concrete creep and shrinkage is ignored.

The ultimate axial load of a composite cross-section in compression is obtained from its axial load-strain curve simulated by the fiber-based model [48]. The moment-curvature relations of the cross-section are required in the nonlinear analysis of CFSST slender columns under eccentric loading. For a given axial load level, the neutral axis depth (d_n) of the composite section is initialized and the strain (ε_t) at the extreme compressive fiber illustrated in Fig. 1 is computed from the given curvature (ϕ) as $\varepsilon_t = \phi d_n$. The material uniaxial stress-strain relations are used to calculate fiber stresses from fiber strains. The axial force in the cross-section is computed as the stress resultant. The neutral axis depth is iteratively adjusted using the secant method [34, 48] or Müller's Method [49, 50] until the internal force is in equilibrium with the external axial load. The internal bending moment is then computed as the stress resultant. The above process is repeated until the complete moment-curvature curve is obtained or the stopping criteria are satisfied [34, 48]. Fig. 2 presents typical moment-curvature curves for the cross-section of a CFSST beam-column.

2.2. Load-deflection analysis

The present study deals with pin-ended slender beam-columns of length *L* subjected to axial load (P) with an eccentricity (*e*) at both column ends as shown in Fig. 3. The slender column has an initial out-of-plane deflection (u_o) at its mid-length. The deflections of the slender column are expressed by the part-sine displacement function.

The displacement control method is employed in the load-deflection analysis of CFSST slender columns. By using this method, the column mid-length deflection (u_m) is incrementally increased and the corresponding axial load *P* is calculated [34, 35]. The column must satisfy the equilibrium condition at its mid-length. The external bending moment at the column mid-length accounting for second order effects and geometric imperfections is computed by

$$M_{me} = P\left(e + u_o + u_m\right) \tag{1}$$

The curvature at the column mid-length can be computed from the displacement by

$$\phi_m = \left(\frac{\pi}{L}\right)^2 u_m \tag{2}$$

For each curvature increment caused by the displacement increment, the corresponding internal axial force and moment can be computed by the axial load-moment-curvature analysis procedures. The internal axial force that satisfies the moment equilibrium at the

column mid-length is determined as the applied axial load *P*. The moment equilibrium condition is expressed in the mathematical form as follows:

$$P\left(e+u_o+u_m\right)-M=0 \tag{3}$$

where M is the internal section moment at the column mid-length.

An iterative numerical procedure is needed to compute the true depth of the natural axis of the composite cross-section as depicted in Fig. 1 until the equilibrium condition at the column mid-length is satisfied. Computational procedures have been proposed by Liang [34, 35] based on the secant method and by Patel et al. [49] and Liang et al. [50] based on Müller's numerical schemes.

2.3. Interaction strength analysis

The axial load-moment strength interaction diagram of a CFSST slender column, which is known as the strength envelope, is used in the design and can also be utilized as a yield surface in the inelastic frame analysis. For the pin-ended slender column under the prescribed axial load (P_n) acting at a varying eccentricity *e* as illustrated in Fig. 3, the analysis method is to determine the maximum moment $(M_{e.\max})$ that could be applied to the column ends. The maximum moment $M_{e.\max}$ is taken as the ultimate moment capacity (M_n) of the slender column. At the column mid-length, the external moment (M_{me}) is written as

$$M_{me}=M_e+P_n\left(u_o+u_m\right) \tag{4}$$

The analysis procedure for computing the strength envelopes of slender CFSST beam-columns is summarized as follows [34].

1. The ultimate axial load (P_{oa}) of the CFSST slender column without bending moments is computed by using the load-deflection analysis procedure described in Section 2.2.
2. Ten load increments are used in the analysis to generate the strength envelope. The load increment is gradually increased from 0.0 to $0.9P_{oa}$ with a load step of $0.1P_{oa}$. This is expressed by $P_n = P_n + \Delta P_n$, where the load increment ΔP_n is set to $0.1P_{oa}$.
3. The curvature at the column mid-length (ϕ_m) is incrementally increased by $\phi_m = \phi_m + \Delta\phi_m$, where $\Delta\phi_m$ is the curvature increment.
4. The column mid-length deflection (u_m) is calculated from the curvature ϕ_m by $u_m = (L/\pi)^2 \phi_m$.
5. The internal moment (M) of the cross-section at the column mid-length under the axial load level P_n is computed by using the moment-curvature analysis procedure.
6. The column end curvatures (ϕ_e) are initialized and adjusted using Müller's numerical technique [49, 50].
7. The column end moment M_e is determined from the curvature ϕ_e by using the moment-curvature analysis procedure.
8. The column end curvatures (ϕ_e) are iteratively adjusted until the moment equilibrium condition at the column mid-length is maintained. This equilibrium condition is expressed by $r_{pm} = M_e + P_n(u_o + u_m) - M = 0$. However, in the numerical analysis, this condition is satisfied if $|r_{pm}| < \varepsilon_k$, where $\varepsilon_k = 10^{-4}$ is the tolerance of convergence.

9. The process of analysis is repeated from Steps 3 to 8 until the column end moment M_e is maximized. This condition is achieved when the external moment (M_{me}) at the column mid-length attains the ultimate section moment capacity of the column under the given axial load.
10. The next load increment is proceeded until the predefined load increment is reached. The process produces a set of ultimate axial loads and moments, which define the strength envelope of the CFSST slender beam-column.

3. Material stress-strain relationships

3.1. Stainless steels

The accurate three-stage stress-strain relations of stainless steels were proposed by Quach et al. [44] that recognize different strain hardening characteristics in tension and compression. Patel et al. [46] reported that there are significant differences between assuming the same and different strain hardening characteristics in tension and compression of stainless steel materials. Their study indicated that the average ultimate axial load of CFSST short columns was underestimated by about 16.9% by using the model that assumes the same strain-hardening behavior in tension and compression when compared to that computed by the model assuming different strain hardening characteristics in tension and compression. Abdella et al. [47] presented an inversion of the three-stage stress-strain model of stainless steels, in which the stress is expressed as a function of the strain. The full-range stress-strain curve for stainless steels is divided into three stages. The first stage is in the strain range of $\varepsilon_s < \varepsilon_{0.2}$; the second stage covers the strain range $\varepsilon_{0.2} < \varepsilon_s \le \varepsilon_{2.0}$; and when $\varepsilon_s > \varepsilon_{2.0}$, the stress-strain curve is in the third stage. In the first stage, stainless steel in compression and tension follows

the same material law. However, in the second and third stages, the stress-strain characteristics in compression are significantly different from those in tension [44] as shown in Fig. 4. The three-stage stress-strain model given by Abdella et al. [47] and Quach et al. [44] is incorporated in the fiber-based technique to simulate the responses of stainless steel materials.

In the first stage $\left(0 \le \varepsilon_s \le \varepsilon_{0.2}\right)$ of the stainless steel stress-strain model, the stresses are calculated from the strains by the following equation [47]:

$$\sigma_s = \frac{E_0\,\varepsilon_s\left[1 + C_1\left(\frac{\varepsilon_s}{\varepsilon_{0.2}}\right)^{C_2}\right]}{1 + C_3\left(\frac{\varepsilon_s}{\varepsilon_{0.2}}\right)^{C_4} + C_1\left(\frac{\varepsilon_s}{\varepsilon_{0.2}}\right)^{C_2}} \tag{5}$$

in which σ_s represents the stainless steel stress, ε_s denotes the stainless steel strain and E_0 represents the modulus of elasticity of stainless steel material, $\varepsilon_{0.2}$ denotes the strain at $\sigma_{0.2}$ and $\sigma_{0.2}$ is the 0.2% proof stress of the stainless steel. The proof strain $\varepsilon_{0.2}$ is given by Ramberg and Osgood [51] as follows:

$$\varepsilon_{0.2} = \frac{\sigma_{0.2}}{E_0} + 0.002 \tag{6}$$

The material parameters C_1, C_2, C_3 and C_4 given in Eq. (5) are calculated by

$$C_1 = \frac{\Delta}{C_2 - 1} \tag{7}$$

$$C_2 = 1 + \frac{B_1}{\Delta} \tag{8}$$

$$C_3 = G_0\left(1 + C_1\right) \tag{9}$$

$$C_4 = \Delta + G_1 \tag{10}$$

where

$$\Delta = \frac{1 + \sqrt{1 + 4B_1}}{2} \tag{11}$$

$$B_1 = \frac{G_1 E_{0.2}\left(n + G_0\right)}{E_0} \tag{12}$$

$$G_0 = \frac{0.002E_0}{\sigma_{0.2}} \tag{13}$$

$$G_1 = \frac{\varepsilon_{0.2} E_{0.2}\left(n - 1\right)}{\sigma_{0.2}} \tag{14}$$

$$E_{0.2} = \frac{E_0}{1 + 0.002\left(\frac{nE_0}{\sigma_{0.2}}\right)} \tag{15}$$

$$n = \frac{\ln\left(20\right)}{\ln\left(\sigma_{0.2}/\sigma_{0.01}\right)} \tag{16}$$

in which $E_{0.2}$ denotes the tangent modulus corresponding to the 0.2% proof strain, and n represents the knee factor determining the sharpness of the knee in the stress-strain curve [51].

In the second stage $(\varepsilon_{0.2} < \varepsilon_s \le \varepsilon_{2.0})$, the stresses in stainless steel are calculated from strains using the Eq. (17) given by Abdella et al. [47]:

$$\sigma_s = \sigma_{0.2} + \frac{E_{0.2}\left[1 + C_5\left(\frac{\varepsilon_s - \varepsilon_{0.2}}{\varepsilon_{1.0} - \varepsilon_{0.2}}\right)^{C_6}\right](\varepsilon_s - \varepsilon_{0.2})}{1 + C_7\left(\frac{\varepsilon_s - \varepsilon_{0.2}}{\varepsilon_{1.0} - \varepsilon_{0.2}}\right)^{C_8} + C_5\left(\frac{\varepsilon_s - \varepsilon_{0.2}}{\varepsilon_{1.0} - \varepsilon_{0.2}}\right)^{C_6}} \tag{17}$$

in which $\sigma_{1.0}$ denotes the 1.0% proof stress and $\varepsilon_{1.0}$ represents the strain at $\sigma_{1.0}$.

Quach et al. [44] suggested that the following equations can be used to compute the 1.0% proof stress $\sigma_{1.0}$ for stainless steels in tension and compression:

$$\sigma_{1.0} = \begin{cases} \sigma_{0.2}\left(\frac{0.662}{n} + 1.085\right) & \text{for compression} \\ \sigma_{0.2}\left(\frac{0.542}{n} + 1.072\right) & \text{for tension} \end{cases} \tag{18}$$

The strain $\varepsilon_{1.0}$ is calculated from $\sigma_{1.0}$ by the following expression [44]:

$$\varepsilon_{1.0} = \varepsilon_{0.2} + \frac{\sigma_{1.0} - \sigma_{0.2}}{E_{0.2}} + \left[0.008 + (\sigma_{1.0} - \sigma_{0.2})\left(\frac{1}{E_0} - \frac{1}{E_{0.2}}\right)\right] \tag{19}$$

The material parameters C_5, C_6, C_7 and C_8 in Eq. (17) are expressed by

$$C_5 = \frac{1}{C_6 - 1} \tag{20}$$

$$C_6 = C_8 + \frac{1}{\ln\left(\frac{\varepsilon_{2.0} - \varepsilon_{0.2}}{\varepsilon_{1.0} - \varepsilon_{0.2}}\right)}\left[\ln(1 + A_2) + \ln\left(\frac{H_0}{H_2}\right)\right] \tag{21}$$

$$C_7 = H_0\left(1 + C_5\right) \tag{22}$$

$$C_8 = 1 + H_1 \tag{23}$$

in which

$$A_2 = \frac{\left(n_2 - 1\right)^2 \left(H_2 - H_0\right)}{\left(1 + n_2 H_0\right)\left(1 + n_2 H_2\right)} \tag{24}$$

$$H_0 = \frac{\left[0.008 + \left(\sigma_{1.0} - \sigma_{0.2}\right)\left(\frac{1}{E_0} - \frac{1}{E_{0.2}}\right)\right] E_{0.2}}{\sigma_{1.0} - \sigma_{0.2}} \tag{25}$$

$$H_1 = \frac{\left(n_2 - 1\right)\left(H_0 + 1\right)}{1 + n_2 H_0} \tag{26}$$

$$H_2 = \frac{E_{0.2}\left(\frac{\varepsilon_{2.0} - \varepsilon_{0.2}}{\varepsilon_{1.0} - \varepsilon_{0.2}}\right)}{\sigma_{2.0} - \sigma_{0.2}} \tag{27}$$

The expression for n_2 in Eq. (24) is given by Quach et al. [44] as

$$n_2 = \begin{cases} 6.399\left(\frac{E_{0.2}}{E_0}\right)\left(\frac{\sigma_{1.0}}{\sigma_{0.2}}\right) + 1.145 & \text{for compression} \\ 12.255\left(\frac{E_{0.2}}{E_0}\right)\left(\frac{\sigma_{1.0}}{\sigma_{0.2}}\right) + 1.037 & \text{for tension} \end{cases} \tag{28}$$

In Eq. (27), $\sigma_{2.0}$ is the 2.0% proof stress and $\varepsilon_{2.0}$ represents the strain at $\sigma_{2.0}$.

Quach et al. [44] provide the following equation to compute the 2.0% proof stress:

$$\sigma_{2.0} = \sigma_{0.2}\left[\frac{1+\left(\frac{\sigma_{1.0}}{\sigma_{0.2}}-1\right)A^{\frac{1}{n_2}}}{1+\left(\frac{\sigma_{0.2}}{E_0}\right)\left(\frac{E_0}{E_{0.2}}-1\right)\left(\frac{\sigma_{1.0}}{\sigma_{0.2}}-1\right)\left(\frac{A^{\frac{1}{n_2}}}{n_2 B_2}\right)}\right] \tag{29}$$

in which

$$A = \frac{B_2}{0.008+\left(\frac{\sigma_{0.2}}{E_0}\right)\left(\frac{\sigma_{1.0}}{\sigma_{0.2}}-1\right)\left(1-\frac{E_0}{E_{0.2}}\right)} \tag{30}$$

$$B_2 = 0.018+\left(\frac{\sigma_{0.2}}{E_0}\right)\left(\frac{E_0}{E_{0.2}-1}\right) \tag{31}$$

The strain $\varepsilon_{2.0}$ is expressed by [44]:

$$\varepsilon_{2.0} = \varepsilon_{0.2}+\frac{\sigma_{2.0}-\sigma_{0.2}}{E_{0.2}}+\left[0.008+\left(\sigma_{1.0}-\sigma_{0.2}\right)\left(\frac{1}{E_0}-\frac{1}{E_{0.2}}\right)\right]\left(\frac{\sigma_{2.0}-\sigma_{0.2}}{\sigma_{1.0}-\sigma_{0.2}}\right)^{n_2} \tag{32}$$

In the third stage $(\varepsilon_{2.0} < \varepsilon_s \le \varepsilon_{su})$, the equation given by Abdella et al. [47] is used to calculate the stresses from the strains as follows:

$$\sigma_s = \frac{A_3 + B_3\varepsilon_s}{1 \pm \varepsilon_s} \tag{33}$$

in which the positive and negative signs indicate the fiber element in tension and compression, respectively.

In Eq. (33), A_3 and B_3 are material constants, which are computed by

$$A_3 = \sigma_{2.0}\left(1+\varepsilon_{2.0}\right) - B_3\varepsilon_{2.0} \tag{34}$$

$$B_3 = \frac{\sigma_{su}\left(1+\varepsilon_{su}\right) - \sigma_{2.0}\left(1+\varepsilon_{2.0}\right)}{\varepsilon_{su} - \varepsilon_{2.0}} \tag{35}$$

in which the ultimate strain ε_{su} and stress σ_{su} can be determined by the following equations presented by Quach et al. [44]:

$$\varepsilon_{uc} = 1 - \frac{1}{1+\varepsilon_{ut}} \tag{36}$$

$$\sigma_{uc} = \left(1+\varepsilon_{ut}\right)^2 \sigma_{ut} \tag{37}$$

in which σ_{ut} is ultimate tensile strength and ε_{ut} is the ultimate tensile strain, and can be written as

$$\sigma_{ut} = \sigma_{0.2}\left[\frac{1-0.0375\left(n-5\right)}{185e_n + 0.2}\right] \tag{38}$$

$$\varepsilon_{ut} = 1 - \frac{\sigma_{0.2}}{\sigma_{ut}} \tag{39}$$

In Eq. (38), e_n is the nondimensional proof stress which is expressed [43] as

$$e_n = \frac{\sigma_{0.2}}{E_0} \tag{40}$$

3.2. Confined concrete

Under applied axial loads, the concrete in a circular CFSST column is subjected to confinement exerted by the circular stainless steel tube. The strength of the concrete in compression as well as its ductility is shown to increase due to the confinement effect [34]. The idealized stress-strain model presented by Liang and Fragomeni [52] for confined concrete in circular CFST columns illustrated in Fig. 5 is utilized for concrete in CFSST columns. The stress-strain relations for confined concrete provided by Mander et al. [53] are adopted in the fiber-based model to describe the parabolic curve from O to A as follows:

$$\sigma_c = \frac{\left(\varepsilon_c / \varepsilon_{cc}^{'}\right)\left(\lambda f_{cc}^{'}\right)}{\left(\varepsilon_c / \varepsilon_{cc}^{'}\right)^{\lambda} + \lambda - 1} \tag{41}$$

$$\lambda = \frac{E_c}{E_c - \left(f_{cc}^{'} / \varepsilon_{cc}^{'}\right)} \tag{42}$$

where σ_c and ε_c are the stress and strain of the confined concrete in compression, $f_{cc}^{'}$ stands for the strength of the confined concrete, $f_c^{'}$ presents the strength of the concrete cylinder, $\varepsilon_{cc}^{'}$ is the strain corresponding to $f_{cc}^{'}$, and E_c is the concrete modulus of elasticity given by ACI 318-11 [4] as

$$E_c = 3320\sqrt{\gamma_c f_c^{'}} + 6900 \quad \left(\text{MPa}\right) \tag{43}$$

in which $\gamma_c = 1.85 D_c^{-0.135}$ $\left(0.85 \le \gamma_c < 1.0\right)$, the reduction factor applied to the strength of the concrete cylinder in compression given by Liang [48], used to consider the column section size effect, and D_c denotes the concrete core diameter.

Mander et al. [53] proposed formulas for computing the strength and strain of the confined concrete in compression, modified by Liang and Fragomeni [52] using γ_c as follows:

$$f_{cc}^{'} = \gamma_c f_c^{'} + 4.1 f_{rp} \tag{44}$$

$$\varepsilon_{cc}^{'} = \varepsilon_c^{'}\left[1 + 20.5\left(\frac{f_{rp}}{\gamma_c f_c^{'}}\right)\right] \tag{45}$$

in which f_{rp} stands for the lateral confining pressure on the concrete, and $\varepsilon_c^{'}$ represents the unconfined concrete strain in compression at the effective compressive strength $\gamma_c f_c^{'}$.

The lateral confining pressure on the concrete core in circular CFSST columns can be computed using the following formulas suggested by Liang and Fragomeni [52] on the basic of the confinement models presented by Tang et al. [54] and Hu et al. [55].

$$f_{rp} = \begin{cases} 0.7\left(v_e - v_s\right)\left(\dfrac{2t}{D-2t}\right)\sigma_{0.2} & \text{for } \dfrac{D}{t} \le 47 \\ \left[6.241\times10^{-3} - 3.5\times10^{-5}\left(\dfrac{D}{t}\right)\right]\sigma_{0.2} & \text{for } 47 < \dfrac{D}{t} \le 150 \end{cases} \tag{46}$$

in which v_e and v_s are Poisson's ratios of the stainless steel tube filled with concrete and of the hollow stainless steel tube [48, 54], respectively. Eq. (46) can be used for both normal and

high strength materials of stainless steel and concrete [52].

The strain $\varepsilon_c^{'}$ is between 0.002 and 0.003, which is a function of the effective strength of the unconfined concrete in compression. When $\gamma_c f_c^{'} \le 28\,\text{MPa}$, $\varepsilon_c^{'}$ is taken as 0.002. When $\gamma_c f_c^{'} > 82\,\text{MPa}$, $\varepsilon_c^{'}$ is 0.003. When $28 < \gamma_c f_c^{'} \le 82\,\text{MPa}$, $\varepsilon_c^{'}$ can be determined by the linear interpolation between 0.002 and 0.003 as suggested by Liang [48].

The straight line AB of the stress-strain model illustrated in Fig. 5 is defined by

$$\sigma_c = f_{cc}^{'}(1-\beta_c)\left(\frac{\varepsilon_{cu}-\varepsilon_c}{\varepsilon_{cu}-\varepsilon_{cc}^{'}}\right)+\beta_c f_{cc}^{'} \quad \left(\varepsilon_{cc}^{'} < \varepsilon_c \le \varepsilon_{cu}\right) \tag{47}$$

in which ε_{cu} is determined to be 0.02 in accordance with experimental evidence [52], and β_c denotes a strength degradation factor applied to the confined concrete in the post-peak range. Hu et al. [55] suggested that when $D/t \le 40$, β_c is taken as 1.0 and when $40 < D/t \le 150$, β_c can be computed by

$$\beta_c = 1.3491 - 1.0085\times10^{-2}\left(\frac{D}{t}\right)+3.39\times10^{-5}\left(\frac{D}{t}\right)^2 \tag{48}$$

For concrete in tension, an idealized stress-strain model is assumed as illustrated in Fig. 5. The model states that the stress of concrete in tension is a linear function of strain before concrete cracking. After concrete cracking, the stress decreases linearly to zero, where the

ultimate strain of concrete in tension is equal to 10 times of the cracking strain. The ultimate strength of concrete in tension is determined as $0.6\sqrt{\gamma_c f_c^{'}}$.

4. Verifications

4.1. Axially loaded circular CFSST slender columns

The experimental performance of eccentrically loaded circular CFSST slender columns has not been investigated and reported in the published literature. Therefore, experimental results on axially loaded circular CFSST slender columns provided by Uy et al. [26] are used to validate the fiber-based model developed. Uy et al. [26] tested twelve circular CFSST columns with column slenderness ratios ranging from 17.1 to 103.5 and *D/t* ratios of 41 and 68. Tested columns were fabricated by using normal or high strength concrete combined with normal strength stainless steel tubes. The geometric and material properties of tested specimens are listed in Table 1. The measurements of initial out-of-plane straightness of tested columns were not undertaken so that they were not included in the inelastic analyses.

The ultimate axial loads ($P_{u.\mathrm{fib}}$) of CFSST columns predicted by the fiber-based model are compared with the measured ultimate axial loads ($P_{u.\mathrm{exp}}$) in Table 1. Good agreement between the fiber element analysis and experimental observation is obtained. The maximum difference between the measured and computed ultimate axial loads is 10% on the safe side, which is acceptable. The mean ratio of $P_{u.\mathrm{fib}} / P_{u.\mathrm{exp}}$ is 0.96. Both the standard deviation and coefficient of variation are calculated as 0.06. The computed and measured deflections of columns C1-1a, C1-2a, C1-2b and C2-2b under axial compression are presented in Figs 6-9. It is shown

that the load-deflection curves of these specimens are accurately captured by the proposed nonlinear fiber-based analysis technique. The post-peak load-deflection characteristics are well predicted.

4.2. Eccentrically loaded circular CFST slender beam-columns

The proposed fiber-based model is further validated by comparisons of numerical results with test data on circular high-strength CFST slender beam-columns presented by Portolés et al. [16] in Tables 2 and 3, where f_y represents the yield strength of carbon steel tubes. The tensile strength of carbon steel tubes was assumed to be 430 MPa. The Young's modulus of carbon steel tubes was taken as 210 GPa. An initial out-of-plane straightness was taken as $L/600$ in the analyses as suggested by Portolés et al. [36]. It is observed that ultimate axial strengths of the beam-columns are reasonably predicted by the fiber-based model. However, the ultimate axial strengths of Specimens C100-3-2-30-20-1 and C100-3-2-30-50-1 are slightly overestimated due to the uncertainty of the actual concrete compressive strength. The mean value of the model-to-experiment ratios is 1.03 and both standard deviation and coefficient of variation are 0.07. The ultimate bending strength $M_{n.\exp}$ in Table 3 was computed as $M_{n.\exp} = P_{n.\exp} \times e$. The fiber-based model predicts well the bending strength of tested beam-columns. The mean predicted-to-tested ratio of ultimate bending strengths is 1.01, and the corresponding standard deviation and coefficient of variation are 0.08.

The predicted load-deflection responses of eccentrically loaded CFST slender beam-columns tested by Portolés et al. [16] are compared with the test results as depicted in Fig. 10. Good agreement between the predicted and experimental load-deflection curves is obtained. It is

seen that in the post-peak range, the experimental response slightly departs from the predicted one. This discrepancy is attributed to the uncertainty of the actual concrete strength.

5. Parametric study

The fiber-based model presented was utilized to analyze eccentrically loaded circular high-strength CFSST slender columns to investigate their structural performance. Important parameters examined were the loading eccentricity ratio (*e/D*), column slenderness ratio (*L/r*), diameter-to-thickness ratio (*D/t*), $f_c^{'}$ and $\sigma_{0.2}$. The initial out-of-plane deflection at the column mid-length was taken as *L*/1000 in the following parametric study.

5.1. Effects of loading eccentricity ratio

The influences of the *e/D* ratio on the structural responses of CFSST slender columns were investigated by undertaking fiber element analyses on columns C1, C2, C3 and C4 given in Table 4. These columns had loading eccentricity ratios varied from 0.1 to 0.6 and 100 MPa high-strength concrete. The computed deflection responses of columns C1, C2, C3 and C4 under eccentric loading are presented in Fig. 11. It is seen that increasing the *e/D* ratio significantly decreases the initial flexural stiffness of the columns. The initial flexural stiffness of the columns with *e/D* ratios of 0.1, 0.2, 0.4 and 0.6 is calculated as 2.033 kN/mm, 1.161 kN/mm, 0.577 kN/mm and 0.394 kN/mm, respectively. However, increasing the *e/D* ratio increases the column mid-length deflection under the ultimate load as well as its displacement-based ductility. Furthermore, the column ultimate axial load is significantly decreased by applying a larger *e/D* ratio as shown in Fig. 12, where P_o is the ultimate axial load of composite cross-section without moments. This is mainly due to the fact that the

column end moments are increased because of the increase in the *e/D* ratio but it reduces the confining pressures on the concrete.

5.2. Effects of column slenderness ratio

The fiber-based analysis technique was utilized to analyze CFSST slender beam-columns C5, C6, C7 and C8 with column slenderness ratios varying from 22 to 100, *D/t* ratio of 50 and $f_c^{'} = 60$ MPa as provided in Table 4. The purpose is to quantify the effects of *L/r* ratio on the performance of CFSST slender beam-columns. Fig. 13 shows the deflection curves for these columns under eccentric loading. The figure demonstrates that increasing the *L/r* ratio results in significant reductions in the initial flexural stiffness and ultimate axial load of CFSST slender columns, but increases the displacement-based ductility of the columns. It is seen from Fig. 13 that under the ultimate axial load, the larger the column slenderness ratio, the larger the column mid-length deflection that can be obtained. This implies that the second order effect is more significant for more slender columns. The dimensionless strength envelopes of columns having *L/r* ratios of 0, 22 and 30 are illustrated in Fig. 14. It appears that increasing the *L/r* ratio reduces the moment capacity of the column under the same axial load level. However, the pure ultimate axial strength and pure moment capacity are not affected by the column slenderness.

5.3. Effects of diameter-to-thickness ratio

The concrete confinement and ductility of a circular CFSST column are a function of its *D/t* ratio. The inelastic analyses were undertaken on columns C9, C10 and C11 with D/t ratios of 40, 70 and 100 detailed in Table 4 to investigate the influences of D/t ratios on their

deflection and strength interaction responses. It is noted that these CFSST columns were constructed by 80 MPa concrete. Fig. 15 shows the computed deflection responses of these columns. It is observed that increasing the D/t ratio considerably reduces the flexural stiffness, significantly decreases the ultimate axial strength, but markedly increases the displacement ductility. The reason for this is that the use of a larger *D/t* ratio of a steel cross-section reduces both its cross-sectional area and confinement effects. When the D/t ratio is increased from 40 to 70 and 100, the increase in the ultimate axial load is computed as 27% and 35%, respectively. The strength envelopes of CFSST columns with different D/t ratios are given in Fig. 16. It appears that the normalized strength interaction diagram tends to enlarge by increasing the D/t ratio. When the D/t ratio of the column is increased from 40 to 70 and 100, the increases in the maximum moment capacity are 38% and 51%, respectively.

5.4. Effects of concrete compressive strengths

As given in Table 4, high-strength concrete with strengths of 60, 90 and 120 MPa was used to construct CFSST slender columns C12, C13 and C14. Nonlinear fiber element analyses were carried out on these high-strength CFSST columns to evaluate the concrete strength effects on their performance. Fig. 17 gives the deflection responses of these CFSST columns under eccentric loading. The numerical results demonstrate that increasing $f_c^{'}$ considerably increases the column flexural stiffness, significantly increases the ultimate axial load but markedly decreases the displacement ductility. The ultimate axial load of the column filled with 90 MPa concrete is 31% higher than the one with 60 MPa concrete. Fig. 18 gives the strength interaction diagrams. The figure illustrates that the strength interaction diagram is enlarged and the maximum moment capacity in the diagram is increased by increasing $f_c^{'}$. When $f_c^{'}$ is

increased from 60 MPa to 120 MPa, an increase of 37% in the maximum moment capacity is expected.

5.5. Effects of stainless steel proof stress

The influence of the stainless steel proof stress on the structural performance of circular high-strength CFSST slender columns was studied by the fiber-based model developed. The CFSST slender columns C15 and C16 listed in Table 4 were analyzed. These two columns were fabricated by stainless steel tubes with proof stresses of 320 and 530 MPa, respectively and filled with 70 MPa high-strength concrete. The predicted deflection of these CFSST slender columns are provided in Fig. 19. It can be seen from the figure that the initial flexural stiffness of the columns is not affected by the proof stress. However, the ultimate axial strength of CFSST columns is shown to increase significantly with increasing the proof stress, and it could increase by 23% if $\sigma_{0.2}$ is increased from 320 to 530 MPa. Fig. 20 illustrates the normalized strength interaction curves. The fiber analysis results indicate that increasing the proof stress significantly increases the pure bending strength. When increasing $\sigma_{0.2}$ from 320 to 530 MPa, the ultimate pure bending moment increases by 46%. Moreover, the maximum ultimate moment capacity of the CFFST columns could be increased considerably by using a stainless steel tube with a higher proof stress.

6. Conclusions

The economical designs of CFSST slender columns can be achieved by utilizing high-strength concrete as infill material. However, experimental and numerical studies on the structural behavior of circular CFSST slender columns of high-strength materials under eccentric

loading have not been conducted previously. An efficient nonlinear fiber-based model has been developed in this paper for calculating the deflection and strength interaction responses of eccentrically loaded circular high-strength CFSST slender columns. The accurate three-stage stress-strain relations of stainless steels that recognize different strain hardening characteristics in tension and compression as well as concrete confinement models have been included in the fiber-based inelastic analysis procedures. The effects of important geometric and material parameters on the responses of circular high-strength CFSST slender columns have been investigated and discussed. It has been demonstrated that the fiber-based inelastic analysis technique developed accurately determines the responses of circular CFSST slender columns. The fiber analysis results obtained from the parametric study have provided a better understanding of the characteristics of circular CFSST slender columns made of high-strength materials.

References

[1] Han LH, Li W, Bjorhovde R. Developments and advanced applications of concrete-filled steel tubular (CFST) structures: Members. J Constr Steel Res 2014;100:211-228.

[2] Eurocode 4 (2004). Design of composite steel and concrete structures–Part 1.1, General rules and rules for buildings. London, UK: British Standards Institution; 2004. BS EN 1994-1-1.

[3] LRFD. Load and resistance factor design specification for steel buildings. American Institute of Steel Construction; 1999.

[4] ACI-318-11. Building code requirements for reinforced concrete. ACI Committee 318, Detroit (MI);2011.

[5] AS 5100.6. Bridge design Part 6: Steel and composite construction, Sydney, New South Wales, Australia: Standards Australia; 2004.

[6] Furlong RW. Strength of steel-encased concrete beam-columns. Journal of the Structural Division, ASCE 1967;93(5):113-24.

[7] Knowles RB, Park R. Strength of concrete-filled steel tubular columns. Journal of the Structural Division, ASCE 1969;95(12):2565-87.

[8] Rangan B, Joyce M. Strength of eccentrically loaded slender steel tubular columns filled with high-strength concrete. ACI Structural Journal 1992;89(6):676-81.

[9] Schneider SP. Axially loaded concrete-filled steel tubes. J Struct Eng, ASCE 1998;124(10):1125-38.

[10] Han LH. Tests on concrete filled steel tubular columns with high slenderness ratio. Advances in Structural Engineering 2000;3(4):337-344.

[11] Varma AH, Ricles JM, Sause R, Lu L-W. Experimental behaviour of high strength square concrete-filled steel tube beam-columns. J Struct Eng, ASCE 2002;128(3):309-327.

[12] Sakino K, Nakahara H, Morino S, Nishiyama I. Behavior of centrally loaded concrete-filled steel-tube short columns. J Struct Eng, ASCE 2004;130(2):180-8.

[13] Fijimoto T. Mukai A, Nishiyama I, Sakino K. Behavior of eccentrically loaded concrete-filled tubular columns. J Struct Eng, ASCE 2004;130(2):203-12.

[14] Giakoumelis G, Lam D. Axial load capacity of circular concrete-filled tube columns. J Constr Steel Res 2004;60(7):1049-68.

[15] Mursi M, Uy B. Behaviour and design of fabricated high strength steel columns subjected to biaxial bending. Part I: Experiments. Adv Steel Constr 2006;2(4):286-315.

[16] Portolés JM, Romero ML, Bonet JL, Filippou FC. Experimental study of high strength concrete-filled circular tubular columns under eccentric loading. J Constr Steel Res 2011;67(4):623-33.

[17] Liew JYR, Xiong DX. Ultra-high strength concrete filled composite columns for multi-storey building construction. Adv Struct Eng 2012;15(9):1487-1503.

[18] Perea T, Leon RT, Hajjar JF, Denavit MD. Full-scale tests of slender concrete-filled tubes: axial behavior. J Struct Eng, ASCE 2013;139(7):1249-62.

[19] Lai Z, Varma AH. Noncompact and slender circular CFT members: Experimental database, analysis and design. J Constr Steel Res 2015;106:220-233.

[20] Aslani F, Uy B, Tao Z, Mashiri F. Behaviour and design of composite columns incorporating compact high-strength steel plates. J Constr Steel Res 2015;107:94-110.

[21] Ren QX, Han LH, Hou C, Hua YX. Experimental behaviour of tapered CFST columns under combined compression and bending. J Constr Steel Res 2017;128:39-52.

[22] Liew JYR, Xiong M, Xiong D. Design of concrete filled tubular beam-columns with high strength steel and concrete. Structures (2016), http://dx.doi.org/10.1016/j.istruc.2016.05.005.

[23] Han LH, Chen F, Liao FY, Tao Z, Uy B. Fire performance of concrete filled stainless steel tubular columns. Eng Struct 2013;56:165-181.

[24] Young B, Ellobody E. Experimental investigation of concrete-filled cold-formed high strength stainless steel tube columns. J Constr Steel Res 2006;62(5):484-92.

[25] Lam D, Gardner L. Structural design of stainless steel concrete filled columns. J Constr Steel Res 2008;64(11):1275-1282.

[26] Uy B, Tao Z, Han LH. Behaviour of short and slender concrete-filled stainless steel tubular columns. J Constr Steel Res 2011;67(3):360-78.

[27] Ellobody E, Ghazy MF. Experimental investigation of eccentrically loaded fiber reinforced concrete-filled stainless steel tubular columns. J Constr Steel Res 2012;76:167-76.

[28] Tokgoz S. Tests on plain and steel fiber concrete-filled stainless steel tubular columns. J Constr Steel Res 2015;114:129-135.

[29] Hajjar JF, Schiller PH, Molodan A. A distributed plasticity model for concrete-filled steel tube beam-columns with interlayer slip. Eng Struct 1998;20(8):663-676.

[30] Susantha KAS, Ge HB, Usami T. Uniaxial stress-strain relationship of concrete confined by various shaped steel tubes. Eng Struct 2001;23(10):1331-1347.

[31] Shanmugam NE, Lakshmi B, Uy B. An analytical model for thin-walled steel box columns with concrete in-fill. Eng Struct 2002;24(6):825-838.

[32] Mursi M, Uy B. Behaviour and design of fabricated high strength steel columns subjected to biaxial bending. Part II: Analysis and design codes. Adv Steel Constr 2006:2(6):314-54.

[33] Hatzigeorgiou GD. Numerical model for the behavior and capacity of circular CFT columns, Part I: Theory. Eng Struct, 2008;30(6):1573-1578.

[34] Liang QQ. High strength circular concrete-filled steel tubular slender beam-columns. Part I: Numerical analysis. J Constr Steel Res 2011;67(2):164-171.

[35] Liang QQ. High strength circular concrete-filled steel tubular slender beam-columns. Part II: Fundamental behavior. J Constr Steel Res 2011;67(2):172-180.

[36] Portolés JM, Romero ML, Filippou FC, Bonet JL. Simulation and design recommendations of eccentrically loaded slender concrete-filled tubular columns. Eng Struct 2011;33(5):1576-93.

[37] Mollazadeh MH, Wang YC. New insights into the mechanism of load introduction into concrete-filled steel tubular column through shear connection. Eng Struct 2014;75 :139–151.

[38] Pagoulatou M, Sheehan T, Dai XH, Lam D. Finite element analysis of the capacity of circular concrete-filled double-skin steel tubular (CFDST) stub columns. Eng Struct 2014;72:102-112.

[39] Ellobody E, Young B. Design and behaviour of concrete-filled cold-formed stainless steel tube columns. Eng Struct 2006;28(5):716-28.

[40] Tao Z, Uy B, Liao FY, Han LH. Nonlinear analysis of concrete-filled square stainless steel stub columns under axial compression. J Constr Steel Res 2011;67(11):1719-32.

[41] Hassanein, MF, Kharoob OF, Liang QQ. Behaviour of circular concrete-filled lean duplex stainless steel-carbon steel tubular short columns. Eng Struct 2013;56:83-94.

[42] Ellobody E. Nonlinear behaviour of eccentrically loaded FR concrete-filled stainless steel tubular columns. J Constr Steel Res 2013;90:1-12.

[43] Rasmussen KJR. Full-range stress-strain curves for stainless steel alloys. J Constr Steel Res 2003; 59(1): 47-61.

[44] Quach WM, Teng JG, Chung KF. Three-stage full-range stress-strain model for stainless steels. J Struct Eng, ASCE 2008;134(9):1518-27.

[45] Gardner L, Nethercot DA. Experiments on stainless steel hollow sections. Part I: Material and cross-sectional behaviour. J Constr Steel Res 2004; 60(9): 1291-1318.

[46] Patel VI, Liang QQ, Hadi MNS. Nonlinear analysis of axially loaded circular concrete-filled stainless steel tubular short columns. J Constr Steel Res 2014;101:9-18.

[47] Abdella K, Thannon RA, Mehri AI, Alshaikh FA. Inversion of three-stage stress–strain relation for stainless steel in tension and compression. J Constr Steel Res 2011;67(5):826-32.

[48] Liang QQ. Performance-based analysis of concrete-filled steel tubular beam-columns. Part I: Theory and algorithms. J Constr Steel Res 2009;65(2):363-72.

[49] Patel VI, Liang QQ, Hadi MNS. High strength thin-walled rectangular concrete-filled steel tubular slender beam-columns. Part I: Modeling. J Constr Steel Res 2012;70:377-384.

[50] Liang QQ, Patel VI, Hadi MNS. Biaxially loaded high-strength concrete-filled steel tubular slender beam-columns. Part I: Multiscale simulation. J Constr Steel Res 2012;75:64-71.

[51] Ramberg W, Osgood WR. Description of stress-strain relations from offset yield strength values. NACA Technical Note no. 927, 1944.

[52] Liang QQ, Fragomeni S. Nonlinear analysis of circular concrete-filled steel tubular short columns under axial loading. J Constr Steel Res 2009;65(12):2186-96.

[53] Mander JB, Priestly MNJ, Park R. Theoretical stress-strain model for confined concrete. J Struct Eng, ASCE 1988;114(8):1804-26.

[54] Tang J, Hino S, Kuroda I, Ohta T. Modeling of stress-strain relationships for steel and concrete in concrete filled circular steel tubular columns. Steel Constr Eng JSSC 1996;3(11):35-46.

[55] Hu HT, Huang CS, Wu MH, Wu YM. Nonlinear analysis of axially loaded concrete-filled tube columns with confinement effect. J Struct Eng, ASCE 2003;129(10):1322-1329.

Figures and Tables

Table 1 Predicted and experimental ultimate axial strengths of axially loaded circular CFSST slender columns.

Specimens	D (mm)	t (mm)	D/t	L (mm)	$\sigma_{0.2}$ (MPa)	E_0 (GPa)	n	$f_c^{'}$ (MPa)	$P_{u.\exp}$ (kN)	$P_{u.\mathrm{fib}}$ (kN)	$\frac{P_{u.\mathrm{fib}}}{P_{u.\exp}}$	Ref.
C1-1a	113.6	2.8	41	485	288.6	173.9	7.6	36.3	738.0	760.24	1.04	[26]
C1-1b	113.6	2.8	41	485	288.6	173.9	7.6	75.4	1137.1	1126.97	0.99	
C1-2a	113.6	2.8	41	1540	288.6	173.9	7.6	36.3	578.9	595.73	1.03	
C1-2b	113.6	2.8	41	1540	288.6	173.9	7.6	75.4	851.1	827.97	0.97	
C1-3a	113.6	2.8	41	2940	288.6	173.9	7.6	36.3	357.6	374.37	1.05	
C2-1a	101	1.48	68	440	320.6	184.2	7.2	36.3	501.3	456.77	0.91	
C2-1b	101	1.48	68	440	320.6	184.2	7.2	75.4	819.0	748.85	0.91	
C2-2a	101	1.48	68	1340	320.6	184.2	7.2	36.3	446.0	403.02	0.90	
C2-2b	101	1.48	68	1340	320.6	184.2	7.2	75.4	692.9	634.20	0.92	
C2-3b	101	1.48	68	2540	320.6	184.2	7.2	75.4	389.7	355.39	0.92	
Mean											0.96	
Standard deviation (SD)											0.06	
Coefficient of variation (COV)											0.06	

Table 2 Predicted and experimental ultimate axial strengths of eccentrically loaded circular CFST slender beam-columns.

Specimens	D (mm)	t (mm)	L (mm)	e (mm)	f_y (MPa)	$f_c^{'}$ (MPa)	$P_{u.\exp}$ (kN)	$P_{u.\mathrm{fib}}$ (kN)	$\frac{P_{u.\mathrm{fib}}}{P_{u.\exp}}$	Ref.
C100-3-2-30-20-1	100	3	2135	20	322	32.70	181.56	210.70	1.16	
C100-3-2-30-50-1	100	3	2135	50	322	34.50	117.49	135.06	1.15	
C100-3-2-70-20-1	100	3	2135	20	322	65.79	248.58	247.52	1.00	
C100-3-2-70-50-1	100	3	2135	50	322	71.64	151.59	150.87	1.00	
C100-3-2-90-20-1	100	3	2135	20	322	95.63	271.04	272.89	1.01	
C100-3-2-90-50-1	100	3	2135	50	322	93.01	154.24	157.57	1.02	
C100-3-3-30-20-1	100	3	3135	20	322	39.43	140.32	150.28	1.07	
C100-3-3-30-50-1	100	3	3135	50	322	36.68	93.75	101.83	1.09	
C100-3-3-70-20-1	100	3	3135	20	322	71.74	159.55	166.26	1.04	
C100-3-3-70-50-1	100	3	3135	50	322	79.55	102.75	112.10	1.09	
C100-3-3-90-20-1	100	3	3135	20	322	94.56	160.33	175.34	1.09	
C100-3-3-90-50-1	100	3	3135	50	322	90.40	106.8	114.16	1.07	
C100-5-2-30-20-1	100	5	2135	20	322	35.39	270.02	288.72	1.07	
C100-5-2-70-50-1	100	5	2135	50	322	30.54	161.26	187.44	1.16	
C100-5-2-70-20-1	100	5	2135	20	322	70.16	313.55	324.80	1.04	
C100-5-2-70-50-1	100	5	2135	50	322	61.00	183.81	203.51	1.11	[16]
C100-5-2-90-20-1	101.6	5	2135	20	320	95.43	330.4	363.55	1.10	
C100-5-2-90-50-1	101.6	5	2135	50	320	81.66	212.17	219.67	1.04	
C100-5-3-30-20-1	101.6	5	3135	20	320	38.67	212.48	215.24	1.01	
C100-5-3-30-50-1	101.6	5	3135	50	320	39.56	144.83	151.70	1.05	
C100-5-3-70-20-1	101.6	5	3135	20	320	71.89	231.35	232.31	1.00	
C100-5-3-70-50-1	101.6	5	3135	50	320	72.49	153.16	161.11	1.05	
C100-5-3-90-20-1	101.6	5	3135	20	320	86.39	246.82	239.03	0.97	
C100-5-3-90-50-1	101.6	5	3135	50	320	96.74	164.95	167.19	1.01	
C125-5-3-90-20-1	125	5	3135	20	322	87.98	474.17	435.06	0.92	
C125-5-3-90-50-1	125	5	3135	50	322	96.97	317.9	300.09	0.94	
C125-5-3-90-20-2[a]	125	5	3135	20	322	107.33	489.47	459.50	0.94	
C125-5-3-90-50-2[a]	125	5	3135	50	322	97.92	322.97	300.65	0.93	
C160-6-3-90-20-1	160.1	5.7	3135	20	322	87.38	1012.5	923.13	0.91	
C160-6-3-70-50-1	160.1	5.7	3135	50	322	74.75	642.16	613.01	0.95	
C160-6-3-90-20-2[a]	160.1	5.7	3135	20	322	83.08	1011.5	910.11	0.90	
Mean									1.03	
Standard deviation (SD)									0.07	
Coefficient of variation (COV)									0.07	

Table 3 Predicted and experimental ultimate bending strengths of eccentrically loaded circular CFST slender beam-columns.

Specimens	D (mm)	t (mm)	L (mm)	e (mm)	f_y (MPa)	$f_c^{'}$ (MPa)	$M_{n.\exp}$ (kNm)	$M_{n.\mathrm{fib}}$ (kNm)	$\frac{M_{n.\mathrm{fib}}}{M_{n.\exp}}$	Ref.
C100-3-2-70-20-1	100	3	2135	20	322	65.79	5.0	4.9	0.98	[16]
C100-3-2-70-50-1	100	3	2135	50	322	71.64	7.6	7.5	0.99	
C100-3-2-90-20-1	100	3	2135	20	322	95.63	5.4	5.5	1.02	
C100-3-2-90-50-1	100	3	2135	50	322	93.01	7.7	7.9	1.03	
C100-5-2-70-20-1	100	5	2135	20	322	70.16	6.3	6.9	1.10	
C100-5-2-90-50-1	101.6	5	2135	50	320	81.66	10.6	11.2	1.06	
C100-5-3-30-50-1	101.6	5	3135	50	320	39.56	7.2	7.9	1.10	
C100-5-3-70-50-1	101.6	5	3135	50	320	72.49	7.7	8.4	1.09	
C100-5-3-90-50-1	101.6	5	3135	50	320	96.74	8.2	8.4	1.02	
C125-5-3-90-50-1	125	5	3135	50	322	96.97	15.9	14.3	0.90	
C125-5-3-90-50-2[a]	125	5	3135	50	322	97.92	16.1	14.2	0.88	
C160-6-3-70-50-1	160.1	5.7	3135	50	322	74.75	32.1	29.4	0.92	
Mean									1.01	
Standard deviation (SD)									0.08	
Coefficient of variation (COV)									0.08	

Table 4 Material and geometric properties of eccentrically loaded circular high strength CFSST beam-columns for parametric study.

Columns	D (mm)	D/t	L/r	e/D	$\sigma_{0.2}$ (MPa)	E_0 (GPa)	n	$f_c^{'}$ (MPa)	$P_{u.\mathrm{fib}}$ (kN)
C1	700	70	30	0.1	320	200	7	100	26851
C2	700	70	30	0.2	320	200	7	100	20804
C3	700	70	30	0.4	320	200	7	100	13087
C4	700	70	30	0.6	320	200	7	100	9063
C5	500	50	22	0.1	320	200	7	60	11456
C6	500	50	40	0.1	320	200	7	60	9907
C7	500	50	70	0.1	320	200	7	60	7292
C8	500	50	100	0.1	320	200	7	60	5104
C9	600	40	30	0.1	530	200	5	80	26912
C10	600	70	30	0.1	530	200	5	80	19727.5
C11	600	100	30	0.1	530	200	5	80	17503
C12	800	80	30	0.1	320	200	7	60	23829
C13	800	80	30	0.1	320	200	7	90	31297
C14	800	80	30	0.1	320	200	7	120	39651
C15	550	55	30	0.1	320	200	7	70	13806
C16	550	55	30	0.1	530	200	5	70	16980

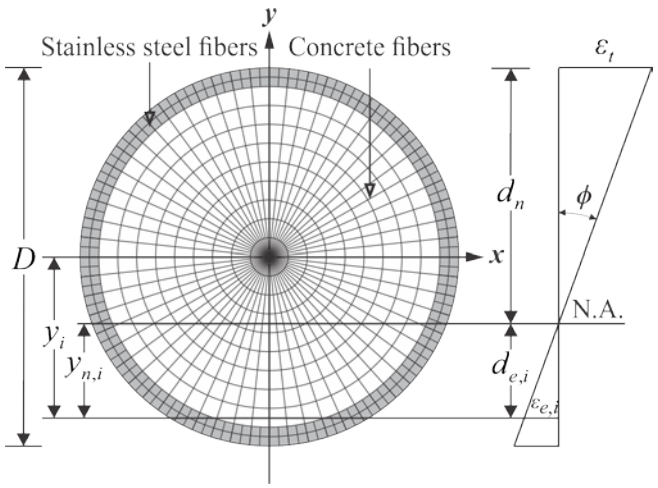

Fig. 1. Typical fiber element discretization of circular cross-section.

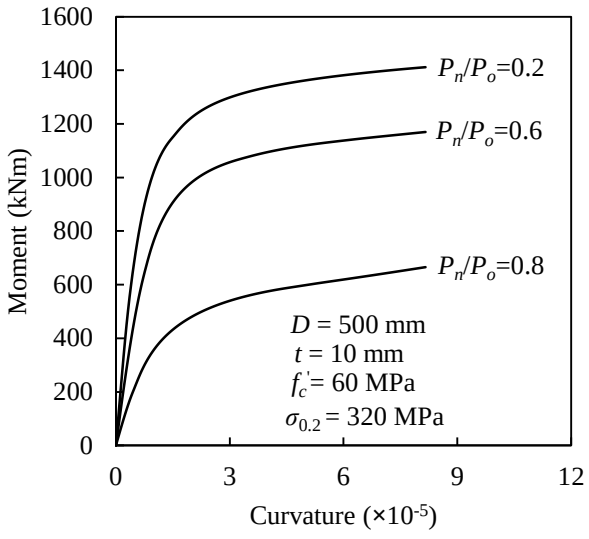

Fig. 2. Moment-curvature curves for the cross-section of a CFSST column.

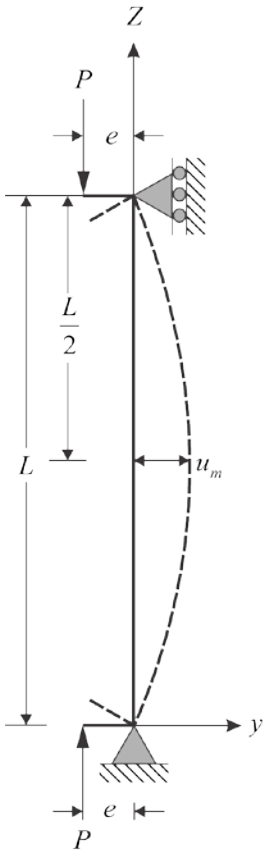

Fig. 3. Pin-ended slender beam-column under eccentric loading.

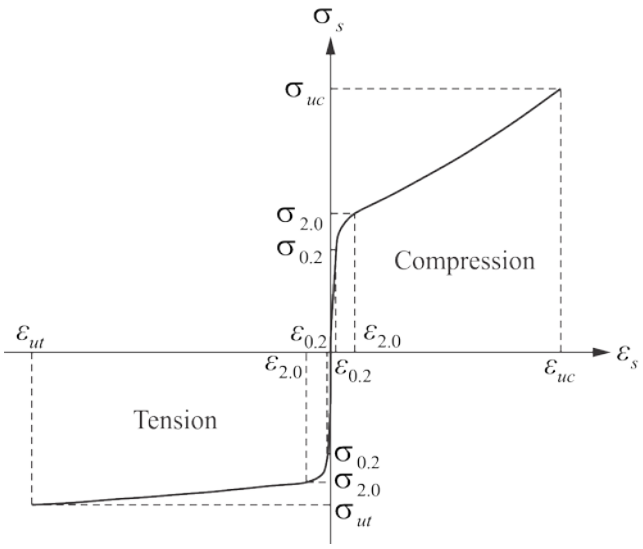

Fig. 4. Three-stage stress-strain curves for stainless steels in tension and compression.

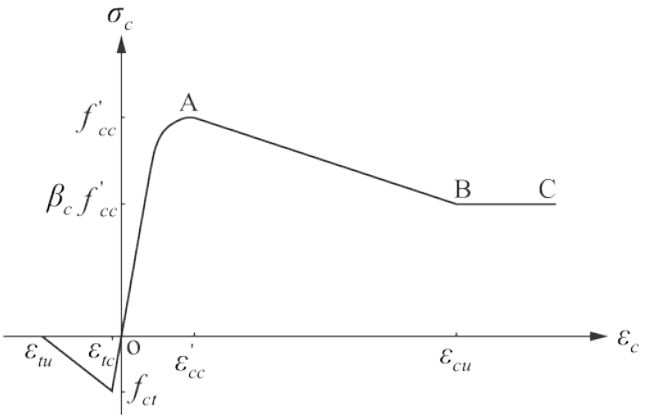

Fig. 5. Stress-strain curves for confined concrete in circular CFSST columns.

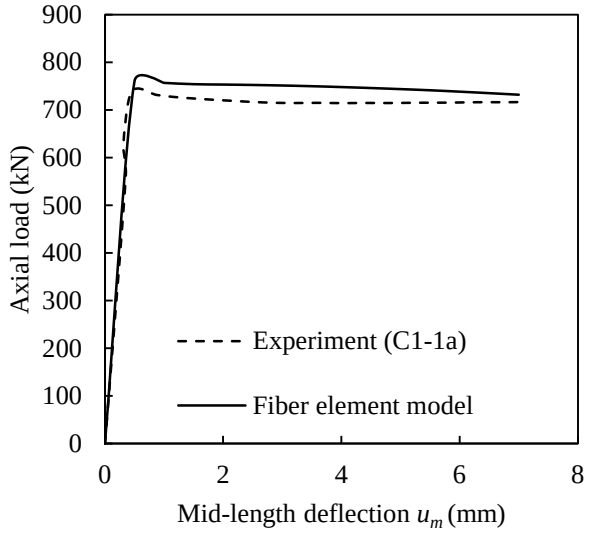

Fig. 6. Comparison of computed and measured load-deflection curves for Specimen C1-1a.

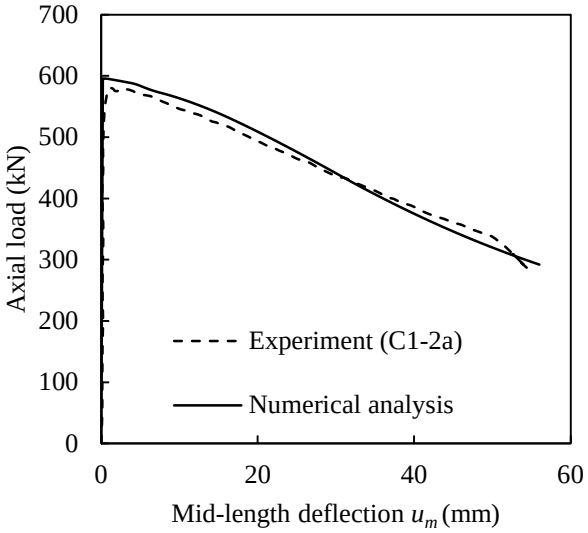

Fig. 7. Comparison of computed and measured load-deflection curves for Specimen C1-2a.

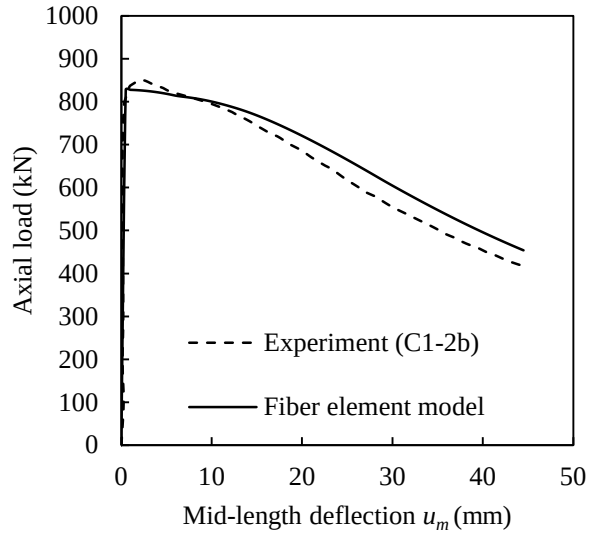

Fig. 8. Comparison of computed and measured load-deflection curves for Specimen C1-2b.

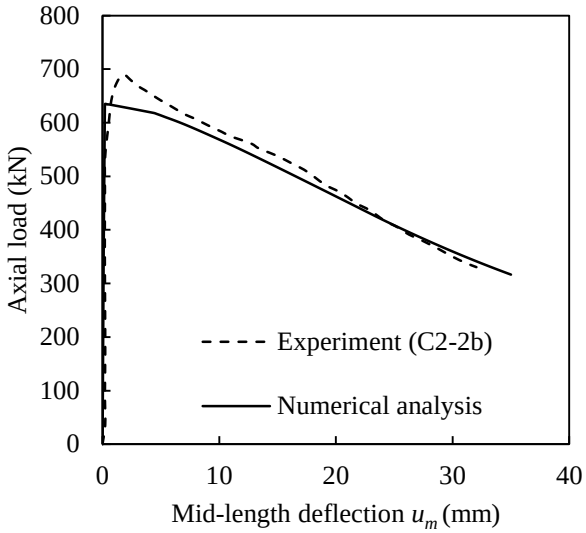

Fig. 9. Comparison of computed and measured load-deflection curves for Specimen C2-2b.

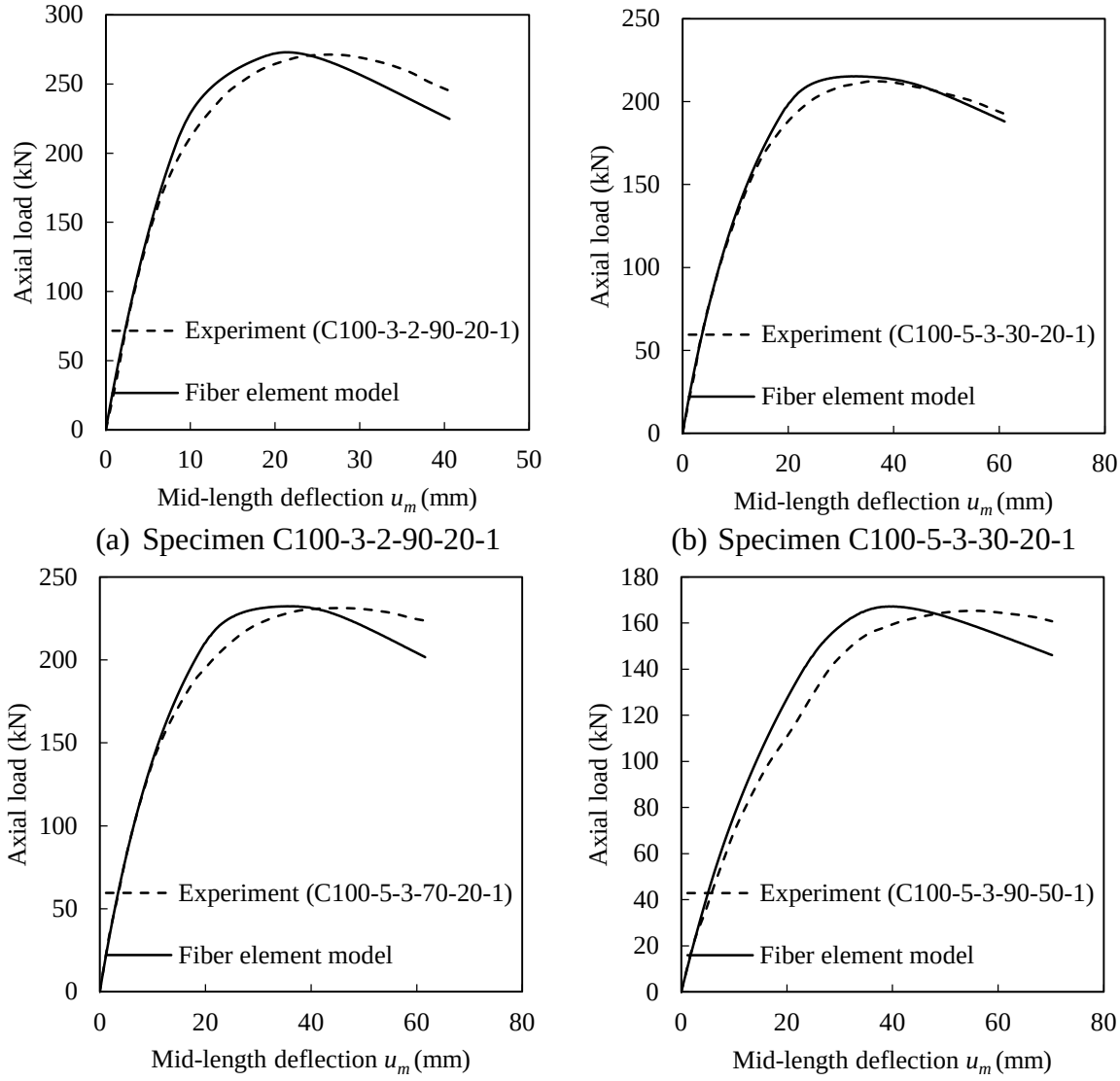

Fig. 10. Comparison of computed and measured load-deflection curves reported by Portolés et al. [16]

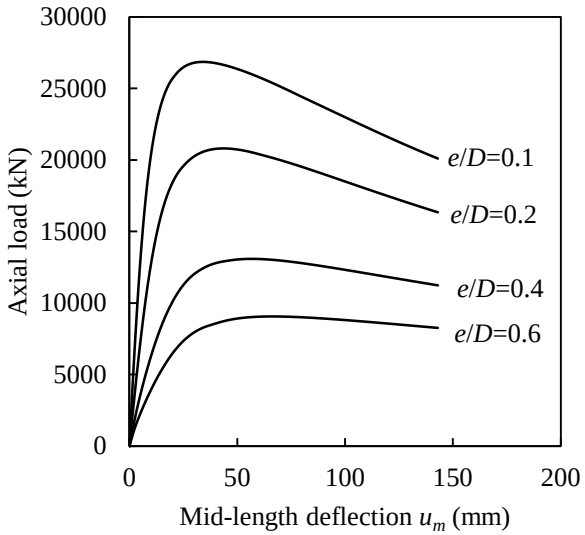

Fig. 11. Load-deflection curves for CFSST slender columns with various *e/D* ratios.

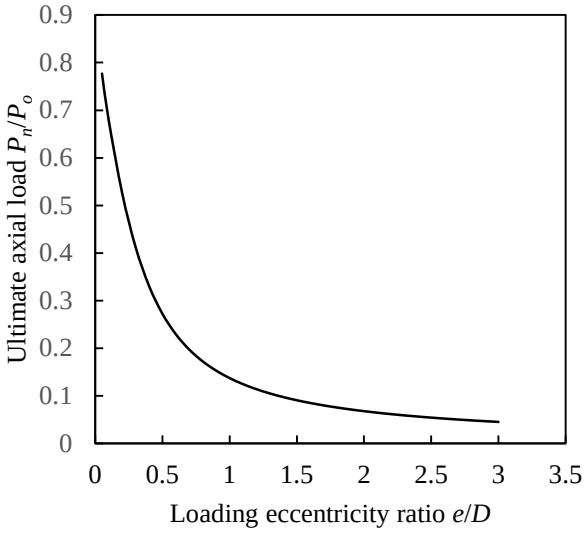

Fig. 12. Normalized ultimate axial load as a function of the eccentricity ratio for CFSST slender columns.

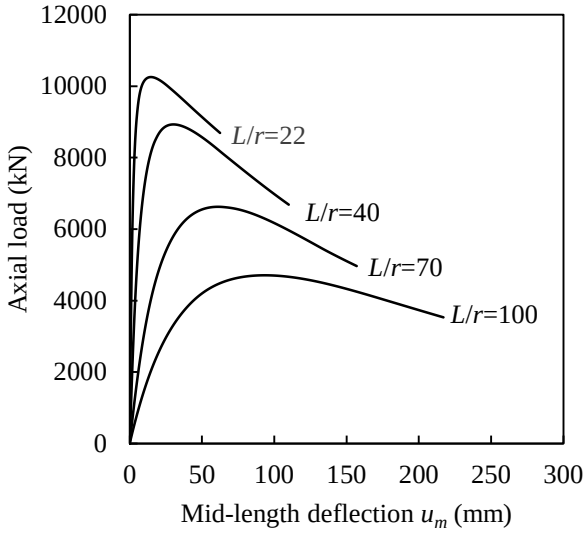

Fig. 13. Load-deflection curves for CFSST slender columns with various *L/r* ratios.

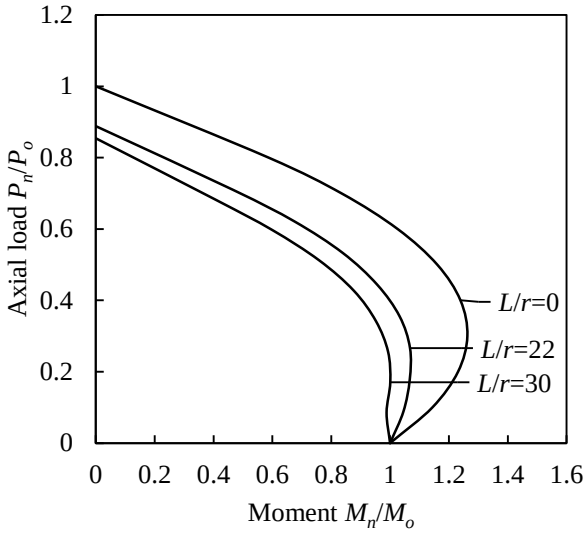

Fig. 14. Strength envelopes of CFSST columns with various *L/r* ratios.

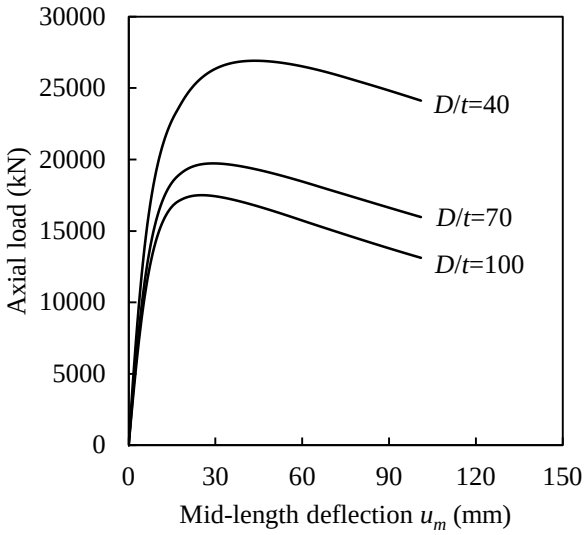

Fig. 15. Load-deflection curves for CFSST slender columns with various D/t ratios.

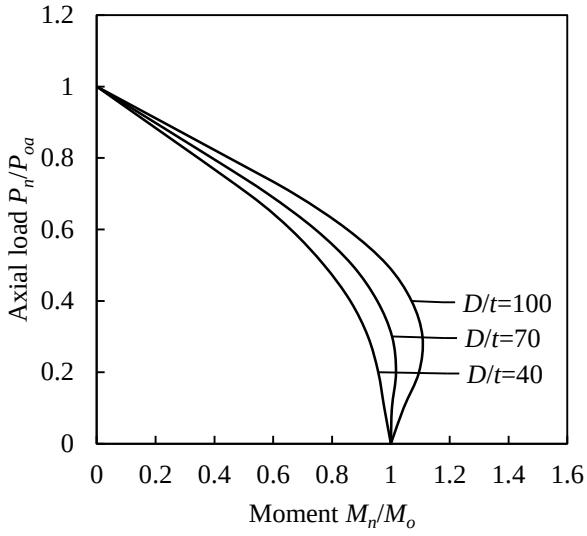

Fig. 16. Strength envelopes of CFSST slender columns with various D/t ratios.

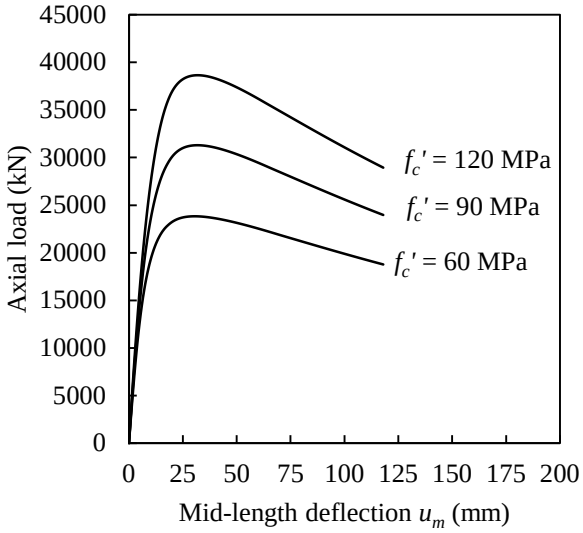

Fig. 17. Load-deflection curves for CFSST slender columns with various concrete strengths.

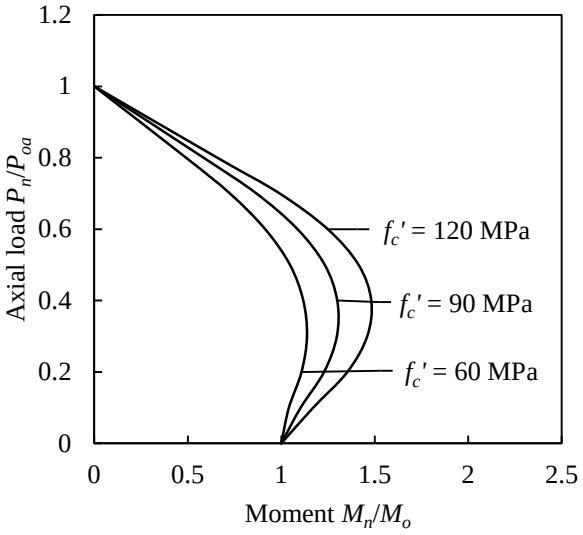

Fig. 18. Strength envelopes of CFSST slender columns with various concrete strengths.

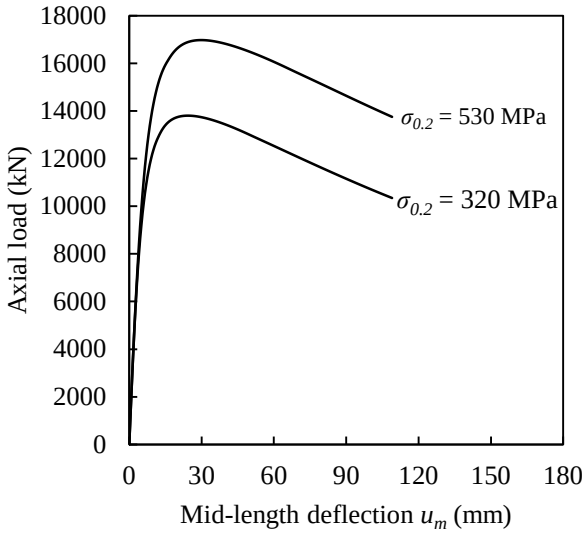

Fig. 19. Load-deflection curves for CFSST slender columns with various stainless steel proof stresses.

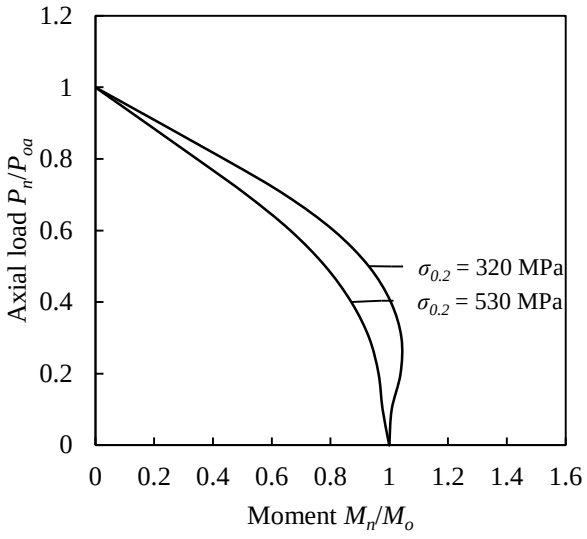

Fig. 20. Strength envelopes of CFSST slender columns with various stainless steel proof stresses.